remote sensing

MDPI

Article

The Surface Heat Flow of Mars at the Noachian–Hesperian Boundary

Javier Ruiz [1,*], Laura M. Parro [2], Isabel Egea-González [3], Ignacio Romeo [1], Julia Álvarez-Lozano [1] and Alberto Jiménez-Díaz [4]

[1] Departamento de Geodinámica, Estratigrafía y Paleontología, Universidad Complutense de Madrid, 28040 Madrid, Spain; iromeobr@ucm.es (I.R.); juliaa07@ucm.es (J.Á.-L.)
[2] Instituto Universitario de Física Aplicada a las Ciencias y las Tecnologías, Universidad de Alicante, 03690 San Vicente del Raspeig, Spain; laura.mparro@ua.es
[3] Departamento de Física Aplicada, Escuela Superior de Ingeniería, Universidad de Cádiz, 11519 Puerto Real, Spain; isabel.egea@uca.es
[4] Departamento de Biología y Geología, Física y Química Inorgánica, ESCET, Universidad Rey Juan Carlos, 28933 Móstoles, Spain; alberto.jimenez.diaz@urjc.es
* Correspondence: jaruiz@ucm.es

Abstract: The time period around the Noachian–Hesperian boundary, 3.7 billionyears ago, was an epoch when great geodynamical and environmental changes occurred on Mars. Currently available remote sensing data are crucial for understanding the Martian heat loss pattern and its global thermal state in this transitional period. We here derive surface heat flows in specific locations based on the estimations of the depth of five large thrust faults in order to constrain both surface and mantle heat flows. Then, we use heat-producing element (HPE) abundances mapped from orbital measurements by the Gamma-Ray Spectrometer (GRS) onboard the Mars Odyssey 2001 spacecraft and geographical crustal thickness variations to produce a global model for the surface heat flow. The heat loss contribution of large mantle plumes beneath the Tharsis and Elysium magmatic provinces is also considered in our final model. We thus obtain a map of the heat flow variation across the Martian surface at the Noachian–Hesperian boundary. Our model also predicts an average heat flow between 32 and 50 mW m^{-2}, which implies that the heat loss of Mars at that time was lower than the total radioactive heat production of the planet, which has profound implications for the thermal history of Mars.

Keywords: surface heat flow; heat loss; heat-producing elements; GRS observations; crustal thickness

Academic Editor: Roberto Orosei

Received: 17 November 2024
Revised: 3 January 2025
Accepted: 7 January 2025
Published: 14 January 2025

Citation: Ruiz, J.; Parro, L.M.; Egea-González, I.; Romeo, I.; Álvarez-Lozano, J.; Jiménez-Díaz, A. The Surface Heat Flow of Mars at the Noachian–Hesperian Boundary. *Remote Sens.* **2025**, *17*, 274. https://doi.org/10.3390/rs17020274

1. Introduction

Mars has very interesting evolutionary, climatic, thermal and geological histories, with different periods characterized by different dynamic and environmental conditions [1–4]. In this sense, the time around the Noachian–Hesperian boundary was an epoch when substantial changes occurred on Mars, including the following: a substantial decrease in aqueous erosion and, therefore, the associated degradation of fluvial features [2,3,5]; a change from abundant phyllosilicate formation to abundant acidic and evaporitic mineralogy [6,7]; a change from olivine-rich volcanism to olivine-pyroxene volcanism [8,9]; a general change in the rock cycle and in the type of crustal rocks [10]; most of the deviation in the topography of the putative ocean's paleo-shorelines [11]; a significant increase in the strength and thickness of the lithosphere and a reduction in the surface heat flow [12]; and maybe the cessation of the Martian dynamo [13–15]. It is hard to think that these changes are coincidental since they all happened at approximately the same time. Therefore, the study of the

dynamics of Mars at this particular time of its history (the Noachian–Hesperian boundary) is crucial in understanding the global evolution of the planet. Because changes in the internal dynamics of Mars can produce modifications in the atmosphere and hydrosphere, as well as changes in the geological expression and external shape of the planet, in general, investigating its thermal state is of great importance for analyzing the sustainability of habitability on Mars and other extraterrestrial worlds [16].

A way of analyzing the internal dynamics of a planet for a given time is through its heat flow. Typically, estimates of heat flow for ancient Mars have been mainly based on the following two geophysical proxies: the effective elastic thickness of the lithosphere (T_e) [17–22] and the depth to the brittle–ductile transition (BDT) beneath large thrust faults [22–29].

Both approaches are based on the relationship between the thermal state of lithospheric rocks and their mechanical strength, and they allow us to calculate the heat flows corresponding to the epoch during which the geological structures used as indicators were formed. While the modeling of both T_e requires topographic and gravity data, the derivation of BDT depths from thrust faults only requires topography information, which is available from orbital data [30,31]. Moreover, the landforms known as lobate scarps, which are the surface expression of large thrust faults, are usually located on terrains with an age close to the Noachian–Hesperian boundary [24,28,29,32–35], and therefore, they give us an opportunity to analyze the global heat flow pattern of Mars during that time.

The modeling of Martian surface heat flows must consider the radioactive heat production in the crust. This has been previously considered in some works calculating ancient local or regional heat flows [21,22,26,28,29,34], and even in deriving a global model for the present-day surface heat flow [36], but it has never been used to build a global model of ancient Mars. The crustal radioactive heat production, which is time-dependent, derives from heat-producing elements (HPEs), which are essentially potassium, thorium and uranium and are incompatible elements with a tendency to accumulate on magma, being more abundant in the uppermost part of the crust. Surface K and Th element abundances were measured by the Gamma-Ray spectrometer aboard the 2001 Mars Odyssey mission [37–39], whereas U abundances had to be estimated based on cosmochemical considerations [40].

In this work, we model the global heat flow pattern, as well as the average heat flow, at the Noachian–Hesperian boundary. We first use fault BDT depths of large thrust faults in the Thaumasia highlands, the circum-Argyre region and close to the dichotomy boundary [29,34,41,42], together with GRS-derived HPEs abundances [39,43], to calculate local heat flows related with the Noachian–Hesperian transition.

We then use the obtained local heat flows, HPE abundances, a crustal thickness model derived from gravity and topography [44], the scaling method developed by Parro et al. [36] and estimates of plume contribution at the Tharsis and Elysium volcanic provinces [45] in order to obtain a global heat flow model (and its associated average heat flow value) for Mars at the Noachian–Hesperian boundary. Finally, we analyze and discuss the implications of our results for the thermal state and evolution of the red planet.

2. Background

Heat flow estimates for the time around the Noachian–Hesperian boundary have been previously proposed for several regions using the BDT depth beneath large thrust falts. These heat flows calculations therefore correspond to the time when the lithosphere was deformed. For example, Grott et al. [20] calculated the heat flow from T_e for Coracis Fossae, which has a formation age of 3.5–3.9 Ga, and obtained a value of 54–66 mW m^{-2}. Later, Grott et al. [24] calculated the heat flow, again in the southern Thaumasia highland region (Warrego rise), from the mechanical modeling of two thrust faults, which are between 4.0 and 3.7 Ga old, obtaining values between 24 and 46 mW m^{-2}. Such differences in heat flow

values derived from near regions and times may be due to the different magmatectonic and thermal environments; the heat flows derived from Coracis Fossae, a magmatically active rift structure, would be higher than the background heat flow values in magmatically inactive areas such as the southern Thaumasia highlands region [24]. These estimations of heat flow were performed without taking into account radioactive heat production from the crust. The presence of radioactive heat sources in the crust is significant, and it should be similar, at least in the uppermost crust, to the amount measured on the Martian surface by the Mars Odyssey Gamma Ray Spectrometer (GRS) [38,43]. Notable, crustal heat production increases the heat flow obtained from lithosphere strength [22].Taking into account crustal HPE abundances, the derived heat flow is 26–44 mW m^{-2} for the Warrego thrust faults [22,26]. These values are similar but somewhat lower than those found by Grott et al. [24] for linear thermal gradients because these authors used faster strain rates and the friction coefficient rather than the stress-dependent coefficient for compression [46]. The most recent estimation of heat flows for that region on Mars (including Phrixi Rupes) was made by Herrero-Gil et al. [34], obtaining a range of heat flow between 24 and 54 mW m^{-2}, using 3D structural modeling on the Warrego faults and obtaining new shallower depths for the BDT.

Around Hellas Planitia, a giant impact 4.0–4.2 Ga old making the deepest depression on Mars [47], several lobate scarps were formed in an age range of a few hundred million years, including the Late Noachian–Early Hesperian boundary, probably related to the crustal thickening and lateral pressure variations following the formation of the basin [28]. The analysis of this set of lobate scarps in the Circum-Hellas region has made the comparison between heat flows in a relatively close area possible, the results being fairly similar (25–39 mW m^{-2}), with the exception of Chalcoporos and Thyles Rupis which give higher values (38–70 mW m^{-2}) and are considered to be less reliable as a result of later topography modifications [28].

Similarly, at the terrains located in Aonia Terra at the NW margin of the Argyre impact basin and parallel to the edge of the Thaumasia Montes, Herrero-Gil et al. [29] modeled the BTD depth of three Late Noachian–Early Hesperian lobate scarps, obtaining heat flows between 25 and 51 mW m^{-2}. The heat flows derived for Bosporos Rupes and Phrixi Rupes are similar to those usually found in the Thaumasia and Circum-Hellas regions; the heat flow obtained for Ogygis Rupes is comparatively higher as a consequence of the lower BDT depth estimated for this lobate scarp. This also suggests that the heat flow derived in the highlands was relatively similar in the Noachian–Hesperian boundary, and in general, heat flows during Late Noachian to Early Hesperian periods are not very high.

The heat flow estimates derived from T_e also give us information about the thermal state of Mars when the lithosphere was loaded [12,19,22,25,48]. The results for structures loaded during the Late Noachian or Early Hesperian periods show a wide dispersion of T_e values, which results in a similarly wide (but badly constrained) dispersion of heat flow values, which could range between ∼10 and ∼100 mW m^{-2}.

3. Thrust Faults Used for the Analysis

To obtain a rough visual of the heat flow of the Martian highlands at the Noachian–Hesperian boundary, we used the BDT depths of five selected lobate scarps associated with large thrust faults (see Figure 1 for locations) formed around the Noachian–Hesperian boundary. These depths give an estimation of the BDT depth at the time of its formation [23,49], and hence, we can use these depths to calculate the heat flow at the time of faulting. We are aware that the true time of faulting may not always coincide with the exact Noachian–Hesperian limit. However, the variations in radioactive heat production rates across time lapses of 10^8 years (comparable to the uncertainty in age determination

for these thrust faults; [24,28,29]) are relatively minor, and there is no evidence of large thermal events during this epoch that could have enhanced the heat flow (rather than the opposed; [12]).

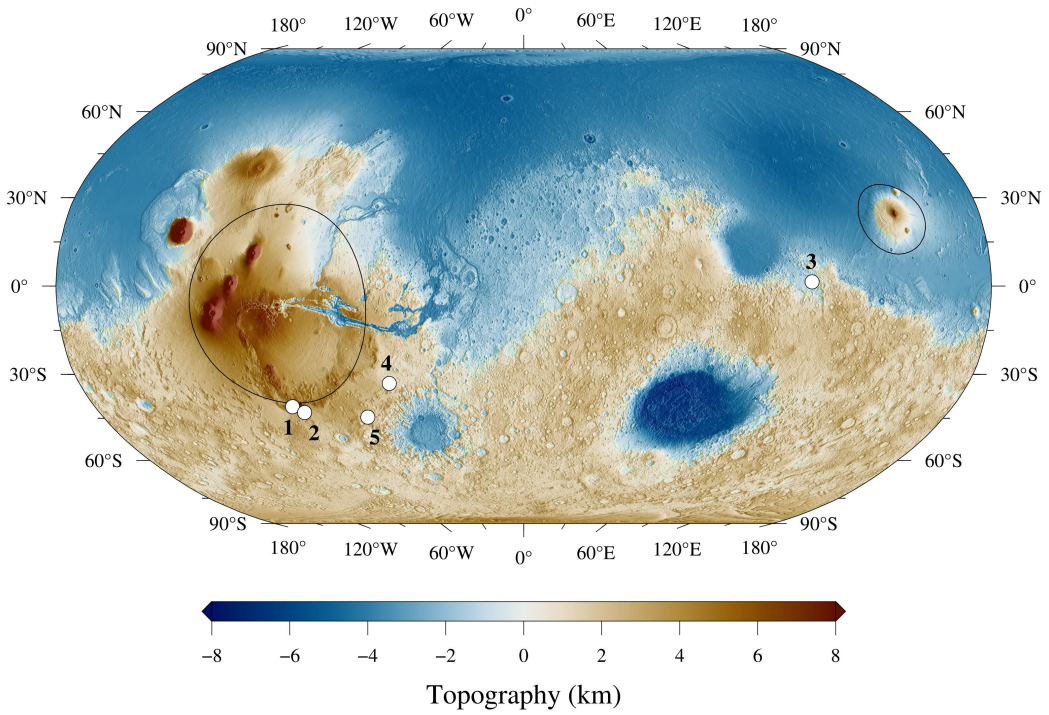

Figure 1. Location of the large thrust faults used in this work (white dots), as well as the rims of the Tharsis and Elysium plume footprints over a Mars Orbiter Laser Altimeter topographic map in Hammer projection. The central meridian is the 0º longitude.

Here, we have used updated BDT depth estimations (Table 1) obtained from the 3D structural reconstructions carried out by Herrero-Gil et al. [34,41,42]. In recent studies, shallower BDT depths were obtained with respect to older works, which should result in higher heat flows. Currently there is no fine 3D modeling available for other thrust faults. This implies a substantial degree of uncertainty exists when calculating mantle average heat flows for Mars (see Section 7.1). The calculations and the models presented here can be easily updated if a higher number of appropriate surface heat flow estimates for the Noachian–Hesperian is made available in the future; this should reduce uncertainties in the average mantle heat flow, and hence, in our final model.

Table 1. Fault parameters, local heat production, surface heat flow intervals and average calculations at 3.7 Ga.

Thrust	BDT Depth (km) [a]	H (μW m^{-3}) [b]	F (mW m^{-2})	b (km) [c]	$F/(bH)$
1. Warrego W	17–21	0.46	53.1–43.9	98.78	1.18–0.98
2. Warrego E	21–27	0.45	43.8–35.8	94.56	1.04–0.85
3. Amenthes Rupes	20–24	0.45	45.8–35.2	58.03	1.76–1.35
4. Ogygis Rupes	17–18	0.39	52.6–49.8	73.48	1.82–1.72
5. Phrixi Rupes	16–19	0.43	56.0–47.7	78.58	1.67–1.42

[a] BDT depth values beneath thrust faults 1, 2 and 5 are from Herrero-Gil et al. [34], 3 from Herrero-Gil et al. [42], and 4 from Herrero-Gil et al. [41]. [b] Local heat production rates for thrust locations are calculated in Section 4. [c] Crustal thickness for thrust locations from the crustal thickness model by [44].

4. HPEs Abundances and Heat Production

Crustal radioactive heat production plays an important role in the elaboration of global models of the surface heat flow distribution of Mars [36]. HPEs are incompatible, which means that these elements tend to be enriched in the crust [50]. Consequently, the mantle should be depleted in these elements, and it should be considered for the estimation of the radioactive production of the lithospheric mantle.

Remote sensing data acquired by the Gamma-Ray Spectrometer (GRS) instrument aboard the Mars Odyssey spacecraft gave us an approximate understanding of the distribution of these elements and their abundances on Mars [37–39,43]. Thus, Mars Odyssey data have been used to determine the abundances of these elements and these are represented in the upper tens of centimeters of the surface, from 10 cm to 1 m below the surface, depending on the density of the underlying material [37]. Maps of the surface abundances of K, Th, and U are shown in Figure 2. Thorium and potassium abundances (Figure 2a,b) were directly measured by the GRS instrument (the most up-to-date data comes from Rani et al. [39]) while we calculated uranium abundances from a Th/U ratio of 3.8 ratio based on Martian meteorite geochemical data [40,51] (converted to surface values in Figure 2c). The GRS data are constrained in latitude (roughly to the ±60° latitudes) due to the high abundance of volatiles (especially water ice) below the surface of the high latitudes of Mars, which has a significant effect on neutron distribution and alters their signal.

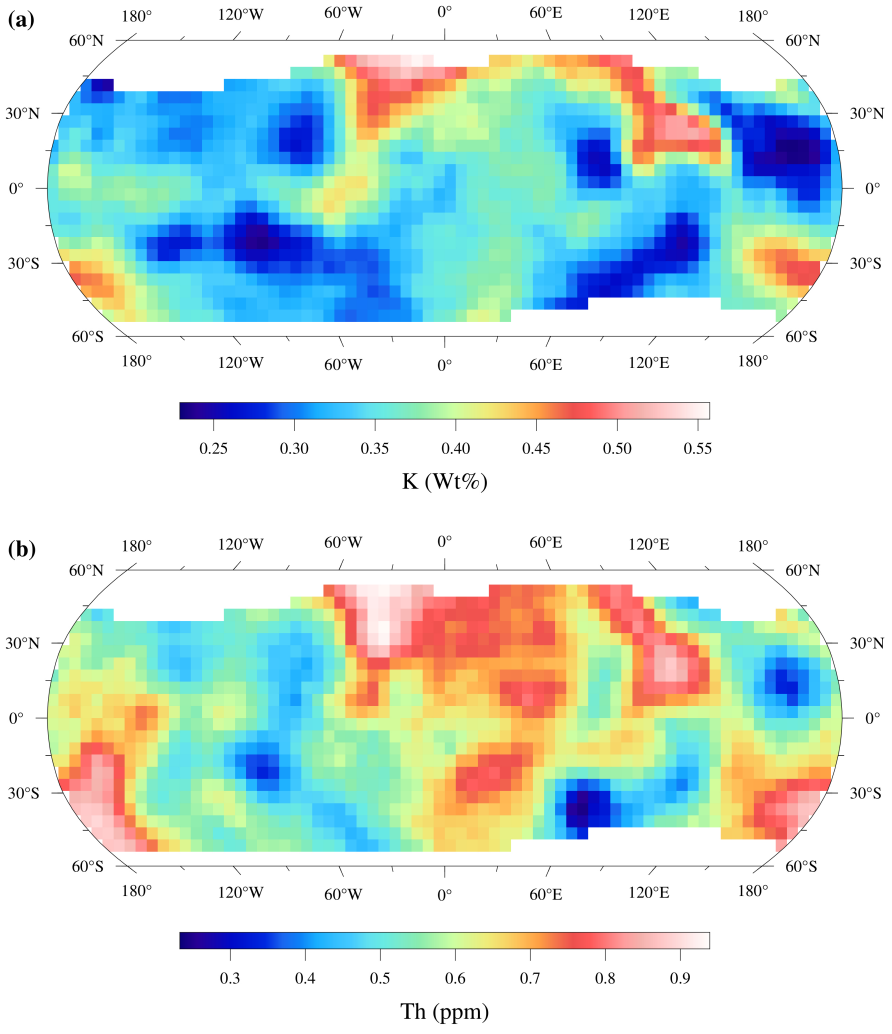

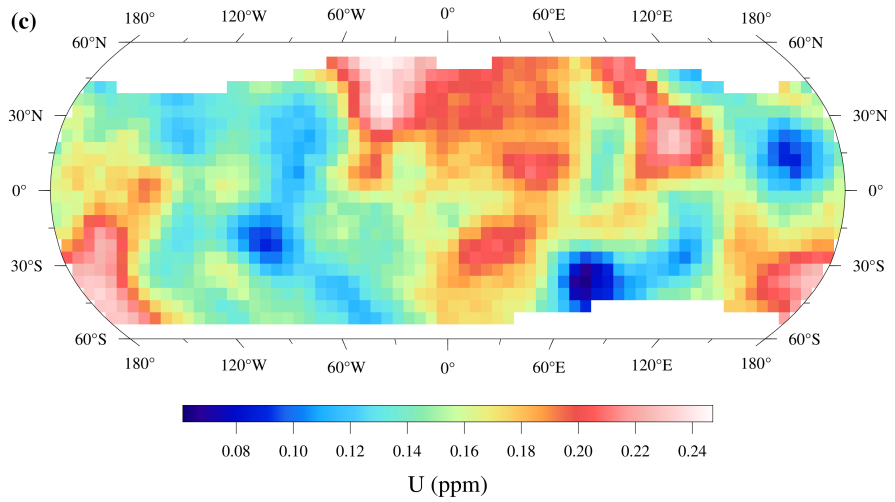

Figure 2. Global smoothed distribution maps of HPE abundances (K, Th and U) on Mars, illustrated with a 5° × 5° per pixel resolution. Base data of K and Th abundances are taken from Rani et al. [39], and the U abundance is calculated from a Th/U ratio of 3.8 [40,51].

The total surface heat production of Mars is the sum of the heat contributions from all HPEs. We calculated the heat production of each radioactive isotope from the standard decay constants in Van Schmus [52] as a function of age. Because the Martian crust is usually considered strongly mixed by cratering [43], we used the observed local HPE abundances to calculate local crustal heat production. For 3.7 Ga, we obtain that H varied from 1.0×10^{-10} W kg^{-1} to 2.5×10^{-10} W kg^{-1} across the planet, with an average value of 1.7×10^{-10} W kg^{-1} (Figure 3).

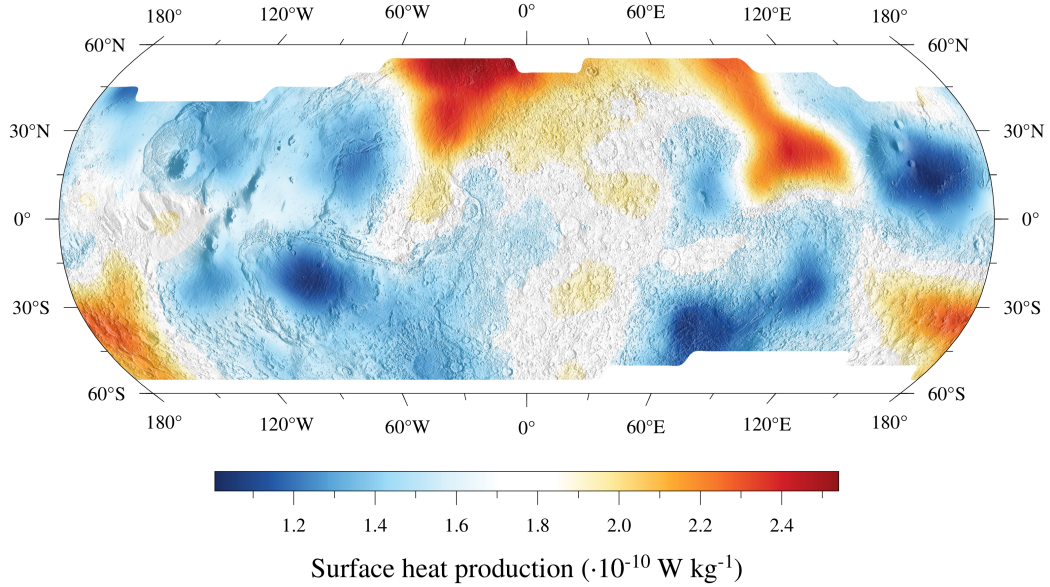

Figure 3. Surface volumetric heat production (H) corresponding to the sum of HPE contributions (K, Th, U) measured by GRS (Mars Odyssey) on Mars, calculated for 3.7 Ga. The data grid is plotted in Hammer projection above the shaded relief of the MOLA topography.

5. Crustal Model

The lateral variations in crustal thickness have a strong influence over the crustal component of the heat flow and, thereby, over the thermal state of the entire lithosphere. Here, we make use of a global uniform-density crustal thickness model of Mars developed by Wieczorek et al. [44], which is constructed from gravity, topography, and seismic constraints.

In particular, the model assumed a uniform crustal density of 2900 kg m^{-3}, with the mantle and core densities taken from the Khan2022 interior model, and the crustal thickness was constrained to be 39 km beneath the InSight lander site (see Wieczorek et al. [44] for details). The crustal thickness model ranges from 6 to 117 km, and the average thickness of the crust is 56.7 km. Table 1 summarizes the local crustal thickness at the location of each lobate scarp.

6. Regional Heat Flows and Crustal HPE Abundances at the Noachian–Hesperian Boundary

In this section, we present heat flow calculations based on the BDT depth estimates of the depth of the five large thrust faults listed in Table 1. We use the same set of thermal and mechanical parameters for all the cases studied here, following the methodology detailed by Ruiz et al. and Egea-Gonzalez et al. [22,28]. This methodology calculates the heat flow from the temperature at the BDT depth (T_{BDT}). Because the ductile strength of the lithosphere depends on temperature, T_{BDT} can be derived by equating the brittle and ductile strength at the BDT, and therefore

$$T_{\mathrm{BDT}} = \frac{Q}{nR}\left[\ln\left(\frac{(1-\lambda)\alpha\rho g Z_{\mathrm{BDT}}}{\left(\frac{\dot{e}}{A}\right)^{1/2}}\right)\right]^{-1}, \quad (1)$$

where Q is the activation energy of the creep, n and A are laboratory-determined constants for creep deformation, R is the gas constant (8.3145 J mol^{-1} K^{-1}), λ is the pore fluid pressure, ρ is the density, α is a coefficient that depends on the stress regime (which takes a value of 3 in the case of thrust faulting; [46]), g is the acceleration due to the gravity (3.72 m s^{-2} for Mars), Z_{BDT} is the BDT depth and $\dot{e}$ is the strain rate. We take λ = 0.35 (valid under hydrostatic conditions), ρ = 2900 kg m^{-3} (following a previous geophysical global modeling of the Martian crust [53–56], the creep parameters for the flow law of the wet diabase of Caristan [57], which are appropriate for a mostly basaltic crust and a wet environment in Late Noachian–Early Hesperian times [58,59]; and a strain rate of 10^{-16} s^{-1}, which is in the upper limit and is considered reasonable for Mars [19,22], suitable for obtaining robust upper limits for the heat flow.

Assuming radioactive heat sources are homogeneously distributed in the crust, the surface heat flow (F) can be calculated from T_{BDT} as

$$F = \frac{k(T_{\mathrm{BDT}} - T_s)}{Z_{\mathrm{BDT}}} + \frac{Z_{\mathrm{BDT}} H}{2}, \quad (2)$$

where k is the thermal conductivity of the crust, T_s is the temperature at the surface, and H is the crustal volumetric heat production rate. We performed the calculations for a constant thermal conductivity of 2 Wm^{-1} K^{-1}, which is appropriated for intact, non-porous basaltic rocks [60], and we assume T_s to be the present mean surface temperature on Mars, 220 K [61]. Regarding the heat produced by radioactive sources, we have opted to use the local heat production for each lobate scarp location, trying to be as faithful as possible to the regional geochemistry of Mars. The local surface heat production values calculated at 3.7 Ga for each thrust fault location varies between 0.39 and 0.46 μW m^{-3} (Table 1).

The obtained surface heat flows are summarized in Table 1. The obtained heat flow values are between 35 and 56 mW m^{-2}. The uncertainty in the obtained heat flows is significant, mainly related to the uncertainty in the modeled fault depths. Our results also provide further information on the compositional stratification of the crust; if we accept that the crustal heat flow component, derived from crustal HPEs and given by bH (where b is the crustal thickness), cannot be higher than the derived surface heat flow (otherwise

the heat flow from the mantle, which includes convective heat flow and radiogenic heat production in the lithospheric mantle, would be negative), then, the ratio $F/(bH)$ makes us aware of any physically unrealistic solutions. For most of the analyzed thrusts, the range of obtained $F/(bH)$ is >1. For two thrusts the range for $F/(bH)$ includes values <1 for this ratio, which would imply negative or very low mantle heat flows. If $F/(bH) < 1$, then HPE abundances cannot be the same in deeper layers as they are in shallower ones.

7. Building a Global Heat Flow Model for 3.7 Ga

7.1. Heat Flow Model Based on Thrust Fault Depths (Mars "Without Plumes")

As the first step in proposing a global heat flow model for Mars at 3.7 Ga, we construct a model following the methodology of Parro et al. [36], which scales crustal thickness variations to heat flow variations through radioactive heat production. This first model still does not take into account the possible influence of the plume activity related to Noachian volcanism. We assume local HPEs are distributed in a HPE-rich upper layer (denoted by $b_{HPEs\text{-}rich}$) and no HPEs exist in the lowermost crust. It can be seen that a $b_{HPEs\text{-}rich}$ of $0.8b$ is consistent with non-negative mantle heat flows in all the thrust fault locations considered in Table 1, which is also consistent with previous studies [26,62–64]. Thus, we assume $b_{HPEs\text{-}rich} = 0.8b$ and modify the scaling procedure by Parro et al. [36] to account for the differentiated crust and local heat production rates. Thus, the local heat flow is given by

$$F = F_{ref} + 0.8\,(bH - b_{ref}H_{ref}), \tag{3}$$

where F_{ref}, b_{ref} and H_{ref} are reference values used for anchoring the model, and b and H are, respectively, the local crustal thickness and heat production rate. The assumption of $b_{HPEs\text{-}rich} = 0.8b$ is conservative, since assuming substantially lower values could imply (if we use an enriched crust thinner than the local BDT depth) the necessity of calculating thermal structures that are more complicated than those described by Equation (2). Furthermore, the ratio $b_{HPEs\text{-}rich}\ /b_c$ could locally vary, but we fit it by necessity. We use b_{ref} = 56.7 km and H_{ref} = 0.49 μW m^{-3} (which is equivalent to the mean radioactive heat produced when considering a density of 2900 kg m^{-3}) as the mean values for Mars. For F_{ref}, we calculated a "mean" heat flow for Mars obtained from

$$F_{ref} = 0.8\,b_{ref}H_{ref} + \overline{F}_{mantle}, \tag{4}$$

where $\overline{F}_{mantle}$ is the mean mantle heat flow deduced from thrust faults (see Table 1). Using $F_{mantle} = F_s - 0.8bH$ and the central F_s values obtained from each trust fault, we obtain $\overline{F}_{mantle}$ = 16.9 ± 9.0 mW m^{-2}. Based on Equation (4), this implies the F_{ref} is between 30 and 48 mW m^{-2}, with a mean value of 39.2 mW m^{-2}, a value that we use for the heat flow model of Mars "without plumes". This model (Figure 4a) shows a heat flow distribution that is greatly related to crustal thickness variations, with larger values (with a maximum of 62 mW m^{-2}) in regions of the southern hemisphere, and lower ones (with a minimum of 19 mW m^{-2}) at the northern plains and large impact basins such as Hellas, Argyre or Isidis Planitiae.

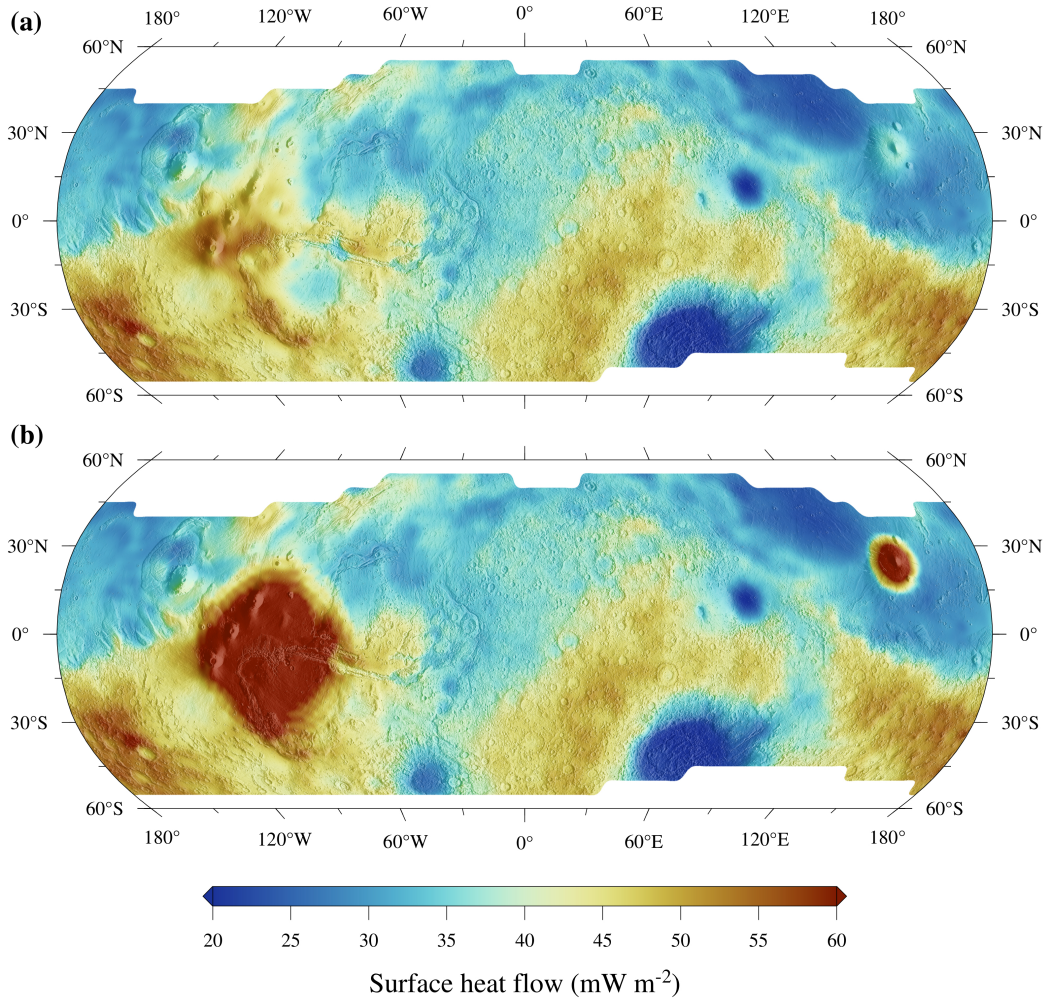

Figure 4. (**a**) Nominal surface heat flow model at 3.7 Ga for Mars in Hammer projection, overlaid on shaded relief map of MOLA topography. (**b**) The same heat flow model but taking into account two large plumes beneath Tharsis and Elysium that add an extra mantle heat flow contribution respect to the model of (**a**). Plume contributions have been calculated assuming a central heat flow of 100 mW m^{-2} and the areas delineated in Figure 1.

7.2. Global Heat Flow Model with Large Plumes

Around the Noachian–Hesperian boundary, the greatest volcanic edifices were forming [65], and the two large volcanic provinces, Tharsis and Elysium, were active. Without plate tectonics, the formation of large volcanoes on Mars is related with the partial melting of the above static mantle plumes [66–71]. In this section we construct a more complete global heat flow model for Mars at 3.7 Ga by adding the contribution of large plumes to the thrust-based model described in the previous section.

For a radial plume, the local plume contribution to the surface heat flow in the areas affected is given by Jellinek et al. [45].

$$F_r = F_{pl}\left[1 - \left(\frac{r}{R}\right)^{1/2}\right], \quad (5)$$

where F_{pl} is the plume heat flow in the center of the plume, r is the distance to the plume center, and R is the radius of the affected area (Plume material spreads radially away from the center and progressively cools towards the rim of the plume footprint [45,72]). We place the center of the plume beneath Tharsis at 6°S, 95°W, corresponding with the center of the demagnetized Tharsis region, as defined by Jellinek et al. [45], but with a radius of

influence of 2000 km, in order to be unaffected the heat flows in the location of the Warrego thrusts, which had similar heat flows to other highlands thrusts (see Table 1). Similarly, we set the center of the Elysium plume at 22.7°N, 145°E, with a 700 km radius for the plume footprint. We assume maximum central heat flows of 100 mW m^{-2} for both mantle plumes; this value corresponds to the maximum calculated by Jellinek et al. [45] for a representative plume for Noachian–Hesperian volcanism, and we are mainly interested in upper limits. Both areas affected by plumes are delineated in Figure 1.

Figure 4b illustrates the heat flow model with the addition of the plume contribution to the first-step model described in the previous section. As expected, the heat flow rises at the points closest to the plume centers, reaching a maximum of 120 mW m^{-2}. However, it is remarkable that, despite the action of the plumes, the reference heat flow (equivalent to the planetary average) in this model is 40.8 mW m^{-2}, only increased by 1.6 mW m^{-2} with respect to the model without plumes. This is because the contribution of a plume rapidly vanished when separated from the plume center. Note that our plume model does not account for small-scale hot spots related to individual volcanoes, which, in any case, would not significantly affect the calculated average heat flow of Mars.

8. Discussion

The proposed global model for the heat flow of Mars at the Noachian–Hesperian boundary provides one approach for estimating the geographical pattern of heat loss, as well as the average heat flow around that time. This could potentially also inform us about the structure of the crust. Indeed, the necessity of avoiding negative mantle heat flows in our calculation of surface heat flows from large thrust faults implies the presence of a a HPE-rich crust that is thinner than the whole crust. As an average, the HPE-rich crust cannot be thicker than 80% of the whole crust, and there must exist a lower HPE-poor crust with a thickness of at least 20% of the whole crust. For an 80% of the crust to be HPE-rich, the assumed average crustal thickness of 56.7 km (see Section 5) implies an equivalent radioactive producing crust of 45.4 km thickness. This is in accordance with previous works that reported a formation of the crust in several stages [62–64] and with works calculating heat from lithosphere strength that found evidence of a heat-producing element (HPE)-enriched upper crust [21,26,28].

Taking into account the influence of the two large mantle plumes below the Tharsis and Elysium magmatic provinces, and given the uncertainty in the mantle heat flow derived from the thrust faults, the average surface heat flows would be between 32 and 50 mW m^{-2} in the Late Noachian–Early Hesperian time. A recent paper by Lee et al. [73] suggests that conductive temperature profiles in the southern highlands could lead, due to their high crustal thickness, to partial melting and intrusive magmatism in the lower crust. Temperature profiles for our average conductive heat flow and the crustal thickness of our nominal model are far from basalt liquidus (see [74]), and therefore, widespread massive melting of the lower crust would not be expected. This suggests that the heat flow in the highlands was comparatively low around the Noachian–Hesperian boundary, what is compatible with heat flow calculations obtained by other works [12,22,28,29]. This result is largely independent of the presence of mantle plumes. Indeed, Figure 5a shows the influence of mantle plume strength on the average planetary heat flow. For mantle plumes with central heat flows below 300 mW m^{-2}, the contributions beneath Tharsis and Elysium were not enough to elevate the average surface heat flow near the total heat production rate generated by the global amount of HPEs (after the composition models of Wanke and Dreibus [75]). As indicated above, mantle plumes with central heat flows above 100 mW m^{-2} are probably unrealistic [45].

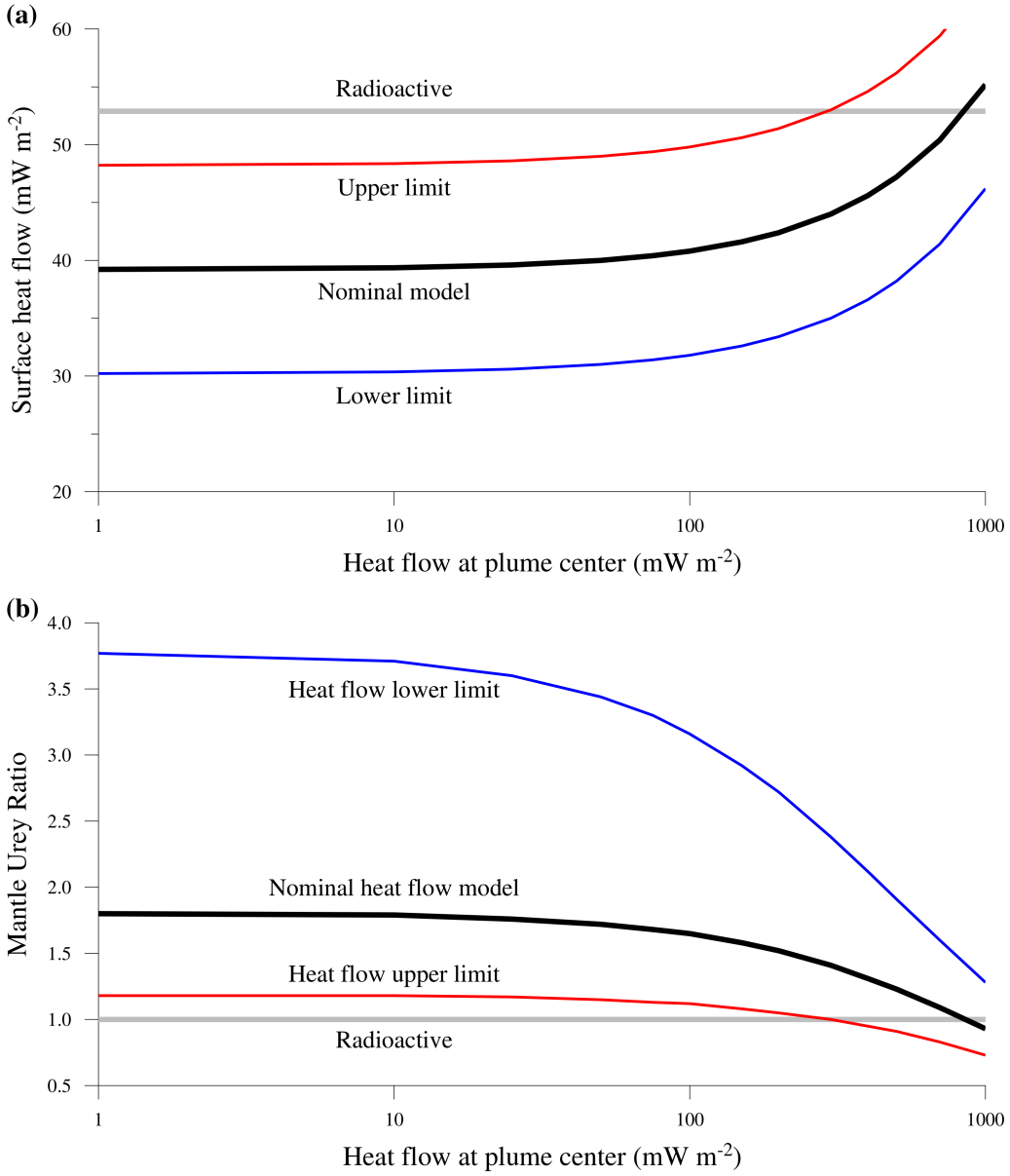

Figure 5. Variations in the average surface heat flow (**a**) and mantle Urey ratio (**b**) as a function of the mantle plume contribution. In both figures, the nominal model corresponds to the average heat flow value of our reference model (40.8 mW m^{-2}), whereas the lower and upper limits cover the uncertainty range (between 32 and 50 mW m^{-2}). The gray line corresponds to the equivalent radioactive component.

A mantle Urey ratio can be defined as the ratio between the total mantle radioactive heat power and the total mantle heat loss used in order to constraint the heat budget of the Martian mantle

$$Ur_M = \frac{H_M}{Q_M}. \quad (6)$$

For $Ur_M < 1$, the mantle as a whole is cooling down or heating up when $Ur_M > 1$. The total radioactive heat production of Mars is not well-known. Thus, we calculated the total radioactive heat power of the mantle from the HPE abundances in the classical global compositional model by Wänke and Dreibus [75], based on the geochemistry of Martian meteorites, and subtracted the crustal radioactive production for an average crust of 56.7 km in thickness, with HPEs distributed only in the upper 80% of its thickness. Due to the uncertainty in the average heat flow calculation, we use the total range obtained

for the calculation of the Urey ratios. The total mantle heat loss is obtained from the average heat flow by subtracting the crustal heat flow component (note that mantle heat loss includes plume effects). Figure 5b shows this relationship with increasing mantle plume contributions, and again, it is observed that this additional mantle heat loss is not enough to be equal to the heat loss with the total radioactive heat power (i.e., $Ur_M > 1$) for reasonable central plume heat flows. This indicates that Mars, at the Noachian–Hesperian boundary, internally produced more heat through radioactivity than the heat it lost through its surface.

The traditional view of the thermal evolution of Mars has considered a substantial heat flow reduction and associated interior cooling with time (e.g., [19,48]), which is mostly related to the high surface-to-volume ratio of this planet. However, there is evidence of low heat flows, and limited interior cooling (or even warming), through much of the history of Mars, deduced from lithosphere strength [12,22]. Moreover, our results support a certain heating of the Martian interior at the Noachian–Hesperian boundary. The heat flow evidence is consistent with deductions on the thermal state of the mantle obtained from the Insight mission (e.g., [76–78]) or from martian meteorites [79]. However, the heat flow was significantly higher in pre-Late Noachian times [12], and therefore, the low global heat flow at the Noachian–Hesperian boundary suggests that Mars experienced a major change in its thermal and geodynamic regime around this time. This change could be related to a reduction in the efficiency of mantle convection, maybe related to inefficient water recycling in the stagnant-lid regime [80,81].

9. Conclusions

The heat flow model of Mars at the Noachian–Hesperian boundary obtained by scaling from local heat flows, derived from thrust faults, and adding the influence of large mantle plumes is one approach for estimating the average heat flow and the heat loss pattern around that time. Our results find average heat flows between 32 and 50 mW m^{-2} for realistic plume strengths. These values are lower than the total radioactive heat production of the planet but consistent with estimates from lithosphere strength or deductions from the interior state using Insight. Because the plume contribution to the whole heat loss of the planets is not enough to change it for realistic scenarios, the conclusion is that the heat flow at 3.7 Ga was low, maybe implying interior heating or the existence of subchondritic heat sources. Because the heat flow was significantly higher in previous Noachian times, the heat flow pattern at the Noachian–Hesperian boundary suggests that Mars experienced a major change in thermal regime around this time, probably related to a lower efficiency of mantle convection.

Author Contributions: Conceptualization, J.R., A.J.-D. and I.E.-G.; methodology, J.R., A.J.-D. and I.E.-G.; software, A.J.-D., I.E.-G. and L.M.P.; validation, J.R. and A.J.-D.; formal analysis, J.R., A.J.-D., I.E.-G., L.M.P. and I.R.; investigation, J.R., A.J.-D., I.E.-G., L.M.P., I.R. and J.Á.-L.; data curation, L.M.P. and A.J.-D.; writing—original draft preparation, J.R., A.J.-D., I.E.-G., L.M.P. and J.Á.-L.; writing—review and editing, J.R., L.M.P., I.E.-G., J.Á.-L. and A.J.-D.; visualization, L.M.P., A.J.-D. and I.E.-G.; supervision, J.R. and A.J.-D.; project administration, J.R.; funding acquisition, J.R. and I.R. All authors have read and agreed to the published version of the manuscript.

Funding: This research has received funding from the projects PID2022-140686NB-I00 (MARVEN), funded by the Spanish Ministry of Science (MICINN); and PR3/23-30839, funded by the Universidad Complutense de madrid. The contribution of L.M.P. was supported by the CIAPOS/2022/066 postdoctoral grant (European Social Fund and Generalitat Valenciana).

Data Availability Statement: The surface heat flow models are available at https://doi.org/10.5281/zenodo.14640773. All figures were generated using the Generic Mapping Tools (GMT) package (https://www.generic-mapping-tools.org/).

Acknowledgments: We thank the comments from two anonymous reviewers.

Conflicts of Interest: The authors declare no conflicts of interest.

References

1. Solomon, S.C.; Aharonson, O.; Aurnou, J.M.; Banerdt, W.B.; Carr, M.H.; Dombard, A.J.; Frey, H.V.; Golombek, M.P.; Hauck, S.A., 2nd; Head, J.W., 3rd; et al. New perspectives on ancient Mars. *Science* **2005**, *307*, 1214–1220. [CrossRef]
2. Carr, M.H.; Head, J.W. Geologic history of Mars. *Earth Planet. Sci. Lett.* **2010**, *294*, 185–203. [CrossRef]
3. Fassett, C.I.; Head, J.W. Sequence and timing of conditions on early Mars. The timing of martian valley network activity: Constraints from buffered crater counting. *Icarus* **2011**, *211*, 1204–1214. [CrossRef]
4. Ramirez, R.M.; Craddock, R.A. The geological and climatological case for a warmer and wetter early Mars. *Nat. Geosci.* **2018**, *11*, 230–237. [CrossRef]
5. Mangold, N.; Adeli, S.; Conway, S.; Ansan, V.; Langlais, B. A chronology of early Mars climatic evolution from impact crater degradation. *J. Geophys. Res.* **2012**, *117*, E04003. [CrossRef]
6. Bibring, J.-P.; Langevin, Y.; Mustard, J.F.; Poulet, F.; Arvidson, R.; Gendrin, A.; Gondet, B.; Mangold, N.; Pinet, P.; Forget, F.; et al. Global mineralogical and aqueous Mars history derived from OMEGA/Mars express data. *Science* **2006**, *312*, 400–404. [CrossRef]
7. Ehlmann, B.L.; Mustard, J.F.; Murchie, S.L.; Bibring, J.-P.; Meunier, A.; Fraeman, A.A.; Langevin, Y. Subsurface water and clay mineral formation during the early history of Mars. *Nature* **2011**, *479*, 53–60. [CrossRef]
8. Baratoux, D.; Toplis, M.J.; Monnereau, M.; Sautter, V. The petrological expression of early Mars volcanism. *J. Geophys. Res.* **2013**, *118*, 59–64. [CrossRef]
9. Wilson, J.H.; Mustard, J.F. Exposures of olivine-rich rocks in the vicinity of Ares Vallis: Implications for Noachian and Hesperian volcanism. *J. Geophys. Res.* **2013**, *118*, 916–929. [CrossRef]
10. McSween, H.Y. Petrology on Mars. *Am. Mineral.* **2015**, *100*, 2380–2395. [CrossRef]
11. Citron, R.I.; Manga, M.; Hemingway, D.J. Timing of oceans on Mars from shoreline deformation. *Nature* **2018**, *555*, 643–646. [CrossRef]
12. Ruiz, J. The early heat loss evolution of Mars and their implications for internal and environmental history. *Sci. Rep.* **2014**, *4*, 4338. [CrossRef] [PubMed]
13. Milbury, C.; Schubert, G.; Raymond, C.A.; Smrekar, S.E.; Langlais, B. The history of Mars' dynamo as revealed by modelling magnetic anomalies near Tyrrhenus Mons and Syrtis Major. *J. Geophys. Res.* **2012**, *117*, E10007.
14. Langlais, B.; Thébault, E.; Quesnel, E.; Mangold, N.A. Late Martian Dynamo Cessation Time 3.77 Gy Ago. *Lunar Planet. Sci. Conf.* **2012**, *43*, 1231.
15. Steele, S.C.; Fu, R.R.; Muxworthy, A.R.; Volk, M.W.R.; Collins, G.S.; North, T.L.; Davison, T.M. Taleomagnetic evidence for a long-lived, potentially reversing martian dynamo at 3.9 Ga. *Sci. Adv.* **2023**, *9*, eade9071. [CrossRef]
16. Ehlmann, B.L.; Anderson, F.S.; Andrews-Hanna, J.; Carter, J.; Catling, D.C.; Christensen, P.R.; Cohen, B.; Dressing, C.D.; Edwards, C.S.; Elkins-Tanton, L.T.; et al. The sustainability of habitability on terrestrial planets: Insights, questions, and needed measurements from Mars for understanding the evolution of Earth-like worlds. *J. Geophys. Res. Planets* **2016**, *121*, 1927–1961. [CrossRef]
17. Solomon, S.C.; Head, J.W. Heterogeneities in the thickness of the elastic lithosphere of Mars: Constraints on heat flow and internal dynamics. *J. Geophys. Res.* **1990**, *95*, 11073–11083. [CrossRef]
18. Anderson, S.; Grimm, R.E. Rift processes at the Valles Marineris, Mars: Constraints from gravity on necking and rate-depending strength evolution. *J. Geophys. Res.* **1998**, *103*, 11113–11124.
19. McGovern, P.J.; Solomon, S.C.; Smith, D.E.; Zuber, M.T.; Simons, M.; Wieczorek, M.A.; Phillips, R.J.; Neumann, G.A.; Aharonson, O.; Head, J.W. Correction to Localized gravity/topography admittance and correlation spectra on Mars: Implications for regional and global evolution. *J. Geophys. Res.* **2004**, *109*, E07007 [CrossRef]
20. Grott, M.; Hauber, E.; Werner, S.C.; Kronberg, P.; Neukum, G. High heat flux on ancient Mars: Evidence from rift flank uplift at Coracis Fossae. *Geophys. Res. Lett.* **2005**, *32*, L21201. [CrossRef]
21. Ruiz, J.; McGovern, P.J.; Tejero, R. The early thermal and magnetic state of the cratered highlands of Mars. *Earth Planet. Sci. Lett.* **2006**, *241*, 2–10. [CrossRef]
22. Ruiz, J.; McGovern, P.J.; Jiménez-Díaz, A.; López, V.; Williams, J.; Hahn, B.C.; Tejero, R. The thermal evolution of Mars as constrained by paleo-heat flows. *Icarus* **2011**, *15*, 508–517. [CrossRef]
23. Schultz, R.A.; Watters, T.R. Forward mechanical modeling of the Amenthes Rupes thrust fault on Mars. *Geophys. Res. Lett.* **2001**, *28*, 4659–4662. [CrossRef]

24. Grott, M.; Hauber, E.; Werner, S.C.; Kronberg, P.; Neukum, G. Mechanical mod- eling of thrust faults in the Thaumasia region, Mars, and implications for the Noachian heat flux. *Icarus* **2007**, *186*, 517–526. [CrossRef]
25. Ruiz, J.; Fernández, C.; Gomez-Ortiz, D.; Dohm, J.M.; López, V.; Tejero, R. Ancient heat flow, crustal thickness, and lithospheric mantle rheology in the Amenthes region, Mars. *Earth Planet. Sci. Lett.* **2008**, *270*, 1–12. [CrossRef]
26. Ruiz, J.; Williams, J.-P.; Dohm, J.M.; Fernández, C.; López, V. Ancient heat flows and crustal thickness at Warrego rise, Thaumasia Highlands, Mars: Implications for a stratified crust. *Icarus* **2009**, *203*, 47–57. [CrossRef]
27. Mueller, K.; Vida, A.; Robbins, S.; Golombek, M.; West, C. Fault and fold growth of the Amenthes uplift: Implications for Late Noachian crustal rheology and heat flow on Mars. *Earth Planet. Sci. Lett.* **2014**, *408*, 100–109. [CrossRef]
28. Egea-González, I.; Jiménez-Díaz, A.; Parro, L.M.; Lopez, V.; Williams, J.P.; Ruiz, J. Thrust fault modeling and Late-Noachian lithospheric structure of the circum-Hellas region, Mars. *Icarus* **2017**, *288*, 53–68. [CrossRef]
29. Herrero-Gil, A.; Egea-González, I.; Ruiz, J.; Romeo, I. Structural modeling of lobate scarps in the NW margin of Argyre impact basin, Mars. *Icarus* **2019**, *319*, 367–380. [CrossRef]
30. Smith, D.; Zuber, M.T.; Frey, H.V.; Garvin, J.B.; Head, J.W.; Muhleman, D.O.; Pettengill, G.H.; Phillips, R.J.; Solomon, S.C.; Zwally, H.J.; et al. Mars Orbiter Laser Altimeter: Experiment summary after the first year of global mapping of Mars. *J. Geophys. Res.* **2001**, *106*, 23689–23722. [CrossRef]
31. Gwinner, K.; Scholten, F.; Preusker, F.; Elgner, S.; Roatsch, T.; Spiegel, M.; Schmidt, R.; Oberst, J.; Jaumann, R.; Heipke, C. Topography of Mars from global mapping by HRSC high-resolution digital terrain models and orthoimages: Characteristics and performance. *Earth Planet. Sci. Lett.* **2010**, *294*, 506–519. [CrossRef]
32. Watters, T.R.; Robinson, M.S. Lobate scarps and the Martian crustal dichotomy. *J. Geophys. Res.* **1999**, *104*, 18981–18990. [CrossRef]
33. Tanaka, K.L.; Robbins, S.J.; Fortezzo, C.M.; Skinner, J.A., Jr.; Hare, T.M. The digital global geologic map of Mars: Chronostratigraphic ages, topographic and crater morphologic characteristics, and updated resurfacing history. *Planet. Space Sci.* **2014**, *95*, 11–24. [CrossRef]
34. Herrero-Gil, A.; Egea-González, I.; Jiménez-Díaz, A.; Rivas-Dorado, S.; Parro, L.M.; Fernández, C.; Ruiz, J.; Romeo, I. Lithospheric contraction concentric to Tharsis: Structural modeling of large thrust faults between Thaumasia highlands and Aonia Terra, Mars. *J. Struct. Geol.* **2023**, *177*, 104983. [CrossRef]
35. Atkins, R.M.; Byrne, P.L.; Wegmann, K.W. Morphometry and timing of major crustal shortening structures on Mars. *Lunar Planet. Sci.* **2019**, *50*, 2132.
36. Parro, L.M.; Jiménez-Díaz, A.; Mansilla, F.; Ruiz, J. Present-day heat flow model of Mars. *Nat. Sci. Rep.* **2017**, *7*, 45629. [CrossRef] [PubMed]
37. Boynton, W.V.; Taylor, G.J.; Evans, L.G.; Reedy, R.C.; Starr, R.; Janes, D.M.; Kerry, K.E.; Drake, D.M.; Kim, K.J.; Williams, R.M.S.; et al. Concentration of H, Si, Cl, K, Fe, and Th in the low and mid latitude regions of Mars. *J. Geophys. Res.* **2007**, *112*, E12S99.
38. Hahn, B.C.; McLennan, S.M.; Klein, E.C. Martian surface heat production and crustal heat flow from Mars Odyssey gamma-ray spectrometry. *Geophys. Res. Lett.* **2011**, *38*, L14203. [CrossRef]
39. Rani, A.; Basu Sarbadhikari, A.; Hood, D.R.; Gasnault, O.; Nambiar, S.; Karunatillake, S. Consolidated chemical provinces on Mars: Implications for geologic interpretations. *Geophys. Res. Lett.* **2022**, *49*, e2022GL099235. [CrossRef]
40. Meyer, C. *Mars Meteorite Compendium*; Lyndon B. Johnson Space Center, NASA: Houston, TX, USA , 2003.
41. Herrero-Gil, A.; Ruiz, J.; Romeo, I. 3D modeling of planetary lobate scarps: The case of Ogygis Rupes, Mars. *Earth Planet Sci. Lett.* **2020a**, *532*, 116004. [CrossRef]
42. Herrero-Gil, A.; Ruiz, J.; Romeo, I. Lithospheric contraction on Mars: A 3D model of the Amenthes thrust fault system. *J. Geophys. Res. Planets* **2020b**, *125*, e2019JE006201. [CrossRef]
43. Taylor, G.J.; Boynton, W.V.; Brückner, J.; Wänke, H.; Dreibus, G.; Kerry, K.E.; Keller, J.M.; Reedy, R.C.; Evans, L.G.; Starr, R.D.; et al. Bulk composition and early differ- entiation of Mars. *J. Geophys. Res.* **2006**, *111*, E03S10.
44. Wieczorek, M.A.; Broquet, A.; McLennan, S.M.; Rivoldini, A.; Golombek, M.; Antonangeli, D.; Beghein, C.; Giardini, D.; Gudkova, T.; Gyalay, S.; et al. InSight constraints on the global character of the Martian crust. *J. Geophys. Res. Planets* **2022**, *127*, e2022JE007298. [CrossRef]
45. Jellinek, A.M.; Johnson, C.L.; Schubert, G. Constraints on the elastic thickness, heat flow, and melt production at early Tharsis from topography and magnetic field observations. *J. Geophys. Res.* **2008**, *113*, E09004. [CrossRef]
46. Ranalli, G. Rheology of the lithosphere in space and time. *Geol. Soc. Spec. Publ.* **1997**, *121*, 19–37. [CrossRef]
47. Frey, H.V. Impact constraints on, and a chronology for, major events in early Mars history. *J. Geophys. Res.* **2006**, *111*, E08S91. [CrossRef]
48. Broquet, A.; Wieczorek, M.A. The gravitational signature of Martian volcanoes. *J. Geophys. Res. Planets* **2019**, *124*, 2054–2086. [CrossRef]
49. Watters, T.R.; Schultz, R.A.; Robinson, M.S.; Cook, A.C. The mechanical and thermal structure of Mercury's early lithosphere. *Geophys. Res. Lett.* **2002**, *29*, 37-1–37-4. [CrossRef]

50. Taylor, S.R.; McLennan, S.M. *Planetary Crusts: Their Composition, Origin and Evolution*; Cambridge University Press: Cambridge, UK, 2009
51. McLennan, S.M. Large-ion lithophile element fractionation during the early differentiation of Mars and the composition of the Martian primitive mantle. *Meteor. Planet. Sci.* **2003**, *38*, 895–904. [CrossRef]
52. Van Schmus, W.R. Natural radioactivity of the crust and mantle. In *Global Earth Physics: A Handbook of Physical constants. AGU Reference Shelf 1*; Ahrens, T.J., Ed.; American Geophysical Union: Washington, DC, USA, 1995; pp. 283–291.
53. Zuber, M.T.; Solomon, S.C.; Phillips, R.J.; Smith, D.E.; Tyler, G.L.; Aharonson, O.; Balmino, G.; Banerdt, W.B.; Head, J.W.; Johnson, C.L.; et al. Nternal structure and early thermal evolution of Mars from Mars Global Surveyor. *Science* **2000**, *287*, 1788–1793. [CrossRef]
54. Neumann, G.A.; Zuber, M.T.; Wieczorek, M.A.; McGovern, P.J.; Lemoine, F.G.; Smith, D.E. The crustal structure of Mars from gravity and topography. *J. Geophys. Res.* **2004**, *109*, E08002. [CrossRef]
55. Genova, A.; Goossens, S.; Lemoine, F.G.; Mazarico, E.; Neumann, G.A.; Smith, D.E.; Zuber, M.T. Seasonal and static gravity field of Mars from MGS, Mars Odyssey and MRO radio science. *Icarus* **2016**, *272*, 228–245. [CrossRef]
56. Wieczorek, M.A.; Beuthe, M.; Rivoldini, A.; Van Hoolst, T. Hydrostatic interfaces in bodies with nonhydrostatic lithospheres. *J. Geophys. Res. Planets* **2019**, *124* [CrossRef]
57. Caristan, Y. he transition from high temperature creep to fracture in Mary- land diabase. *J. Geophys. Res.* **1982**, *87*, 6781–6790. [CrossRef]
58. Parmentier, E.M.; Zuber, M.T. Early evolution of Mars with mantle compositional stratification or hydrothermal crustal cooling. *J. Geophys. Res.* **2007**, *112*, E02007. [CrossRef]
59. Andrews-Hanna, J.C.; Phillips, R.J.; Zuber, M.T. Meridiani Planum and the global hydrology of Mars. *Nature* **2007**, *446*, 163–165. [CrossRef]
60. Beardsmore, G.R.; Cull, J.P. *Crustal Heat Flow: A Guide to Measurement and Modelling*; Cambridge University Press: Cambridge, UK, 2001; p. 324.
61. Kieffer, H.H.; Martin, T.Z.; Peterfreund, A.; Jakosky, B.M.; Miner, E.; Palluconi, F.D. Thermal and albedo mapping of Mars during the Viking primary mission. *J. Geophys. Res.* **1977**, *82*, 4249–4291. [CrossRef]
62. Norman, M.D. The composition and thickness of the crust of Mars estimated from rare Earth elements and neodymium-isotopic compositions of martian meteorites. *Meteor. Planet. Sci.* **1999**, *34*, 439–449. [CrossRef]
63. Norman, M.D. hickness and composition of the martian crust revisited: Implications of an ultradepleted mantle with Nd isotopic composition like that of QUE94201. *Lunar Planet. Sci.* **2002**, *33*, 1175.
64. Grott, M. Late crustal growth on Mars: Evidence from lithospheric extension. *Geophys. Res. Lett.* **2005**, *32*, L23201. [CrossRef]
65. Werner, S.C. The global martian volcanic evolutionary history. *Icarus* **2009**, *201*, 44–68. [CrossRef]
66. Carr, M.H. Volcanism on Mars. *J. Geophys. Res.* **1973**, *78*, 4049–4062. [CrossRef]
67. McKenzie, D.; Barnett, D.; Yuan, D.-N. The relationship between martian gravity and topography. *Earth Planet. Sci. Lett.* **2002**, *195*, 1–16. [CrossRef]
68. Wenzel, M.J.; Manga, M.; Jellinek, M. Tharsis as a consequence of Mars' dichotomy and layered mantle. *Geophys. Res. Lett.* **2004**, *31*, L04702. [CrossRef]
69. Belleguic, V.; Lognonne, P.; Wieczorek, M. Constraints on the martian lithosphere from gravity and topography data. *J. Geophys. Res.* **2005**, *110*, E11005. [CrossRef]
70. Cohen, B.E.; Mark, D.F.; Cassata, W.S.; Lee, M.R.; Tomkinson, T.; L, C. Smith Taking the pulse of Mars via dating of a plume-fed volcano. *Nat. Commun.* **2017**, *8*, 640. [CrossRef]
71. Day, J.M.D.; Tait, K.T.; Moynier, F.; Neal, C.R.; Liu, Y.; Udry, A. Martian magmatism from plume metasomatized mantle. *Nat. Commun.* **2018**, *9*, 4799. [CrossRef] [PubMed]
72. Grott, M.; Breuer, D. On the spatial variability of the martian elastic lithosphere thickness: Evidence for mantle plumes? *J. Geophys. Res.* **2008**, *115*, E03005. [CrossRef]
73. Lee, C.-T.; Keller, D.; Dasgupta, R.; Siebach, K.; McGovern, P.; Borchardt, J.; Zhang, J. Crustal thickness effects on chemical differentiation and hydrology on Mars. *Earth Planet. Sci. Lett.* **2025**, *651*, 119155. [CrossRef]
74. Schmidt, M.W.; Poli, S. Experimentally based water budgets for dehydrating slabs and consequences for arc magma generation. *Earth Planet. Sci. Lett.* **1998**, *163*, 361–379. [CrossRef]
75. Wänke, H.; Dreibus, G. Chemical composition and accretion history of terrestrial planets. *Philos. Trans. R. Soc. Lond.* **1988**, *325*, 545–557.
76. Drilleau, M.; Samuel, H.; Garcia, R.F.; Rivoldini, A.; Perrin, C.; Michaut, C.; Wieczorek, M.; Tauzin, B.; Connolly, J.A.D.; Meyer, P.; et al. Marsquake locations and 1-D seismic models for Mars from InSight data. *J. Geophys. Res. Planets* **2022**, *127*, e2021JE007067. [CrossRef] [PubMed]
77. Samuel, H.; Drilleau, M.; Rivoldini, A.; Xu, Z.; Huang, Q.; Garcia, R.F.; Lekić, V.; Irving, J.C.E.; Badro, J.; Lognonné, P.; et al. Geophysical evidence for an enriched molten silicate layer above Mars's core. *Nature* **2023**, *622*, 717–718. [CrossRef] [PubMed]

78. Khan, A.; Huang, D.; Durán, C.; Sossi, P.A.; Giardini, D.; Murakami, M. Evidence for a liquid silicate layer atop the Martian core. *Nature* **2023**, *622*, 718–723. [CrossRef]
79. Hernández-Montenegro, J.D.; Asimow, P.D.; Herzberg, C.T. Estimating primary magmas from Mars with PRIMARSMELT: Implications for the petrogenesis of some Martian rocks and the thermal evolution of Mars. *J. Geophys. Res. Planets* **2024**, *129*, e2024JE008508. [CrossRef]
80. McGovern, P.J.; Schubert, G. Thermal evolution of the Earth: Effects of volatile exchange between atmosphere and interior. *Earth Planet. Sci. Lett.* **1989**, *96*, 27–37. [CrossRef]
81. Sandu, C.; Kiefer, W.S. Degassing history of Mars and the lifespan of its magnetic dynamo. *Geophys. Res. Lett.* **2012**, *39*, L03201. [CrossRef]